

Orbital structure in barred galaxies

N. Voglis, ^{*} M. Harsoula and G. Contopoulos

Research Center for Astronomy and Applied Mathematics, Academy of Athens, Soranou Efessiou 4, GR-115 27 Athens, Greece
e-mail: mharsoul@academyofathens.gr, gcontop@academyofathens.gr

Released 2007 April 12

ABSTRACT

We study the orbital structure of a self-consistent N-body equilibrium configuration of a barred galaxy constructed from cosmological initial conditions. The value of its spin parameter λ is near the observed value of our Galaxy $\lambda = 0.22$. We classify the orbits in regular and chaotic using a combination of two different methods and find 60% of them to be chaotic. We examine the phase space using projections of the 4D surfaces of section for test particles as well as for real N-body particles. The real particles are not uniformly distributed in the whole phase space but they avoid orbits that do not support the bar. We use frequency analysis for the regular orbits as well as for the chaotic ones to classify certain types of orbits of our self-consistent system. We find the main resonant orbits and their statistical weight in supporting the shape of the bar and we emphasize the role of weakly chaotic orbits in supporting the boxiness at the end of the bar.

Key words: galaxies:structure, kinematics and dynamics.

1 INTRODUCTION

The type of orbits that appear in various types of galaxies have been studied extensively up to now. (For a review see Contopoulos 2002). However relatively few studies have been made on the orbital structure of N-body systems (see for example Sparke & Sellwood (1987), Sundin et al. (1993), Sundin (1996), Miwa and Noguchi (1998), Barnes and Tohline (2001), Shen & Sellwood (2004), Ceverino & Klypin (2005)). In this paper we consider a N-body model of a triaxial barred galaxy. Its spin parameter is relatively large, comparable to the spin parameter of our Galaxy. Our study aims to find the main types of orbits in such a galaxy. We emphasize the chaotic orbits that are 60% of the totality, in contrast with non-rotating N-body systems where the chaotic orbits are only 30%. The chaotic orbits occupy most of the space outside corotation. However the chaotic orbits are not completely mixed. They are separated for long times by cantori. Relatively few chaotic orbits escape from the system during a Hubble time.

There are also many ordered orbits of various resonant types, mainly inside the bar. The topology of the orbits is governed by the resonances between the rotational and the

epicyclic frequencies. The third dimension plays a minor role on the type of orbits.

A comparison between the N-body orbits and the orbits of test particles in the same potential shows that real orbits avoid systematically certain types of resonant orbits, occupying preferentially orbits that support the bar. In fact models consisting of particles uniformly distributed initially are not self-consistent.

The paper is organized as follows: In section 2 we describe the method used for constructing a realistic bar model and in section 3 we describe the characteristic features of the bar. Section 4 discusses the level of chaos. Section 5.1 describes the various types of orbits by using surfaces of section and section 5.2 introduces a frequency analysis of the orbits. Finally in section 6 we summarize our conclusions.

2 COSMOLOGICAL INITIAL CONDITIONS FOR CREATING A BAR-LIKE GALAXY

For creating the final configuration of a bar-like galaxy we have used two different N-body codes: a tree code developed by Hernquist (1988) and a conservative technique code designed by Allen et al. (1990). Initially 5616 particles of equal mass are positioned in a cubic grid limited by a sphere and having a total mass equal to the mass of a galaxy. The system expands initially according to an Einstein-de Sitter model universe and then we impose a density perturbation with a spherical profile and a power law dependence on the radius r , i.e.

^{*} This work started by Dr. N. Voglis with Dr. M. Harsoula. It was very sad that Dr. Voglis passed away suddenly on 9/2/2007. After that Dr. G. Contopoulos continued this work and completed this paper in collaboration with Dr. M. Harsoula.

$$s(r) = \frac{\delta\rho}{\rho} \approx \frac{1}{r^{(n+3)/2}} \quad (1)$$

Such a profile is consistent with a power-law spectrum of the density perturbation in the early Universe. Here we set $n = -2$, a value that is in the range predicted by the Cold Dark Matter scenario for galactic mass scales (Davis et al. 1985). Further details for these "quiet initial conditions" can be found in Voglis (1994). The unit length is $1kpc$, and the unit of time $t_{unit}=1Myr$ while the total mass is taken as $10^{12}M_{\odot}$. Using the tree code, we find that the violent relaxation process has been completed after $t = 4000t_{units}$. Then we split each particle into 27 particles arranged in a small cubic grid, while the sum of these children particles conserves the mass, energy and angular momentum of the parent particle. The new configuration consists of about 1.4×10^5 particles and is now put as initial condition for the new run using the conservative technique code (hereafter c-t) for another 150 half-mass crossing times. The c-t code gives a smooth potential containing 120 terms (monopole, quadrupole and triaxial). All the details are given in Kalapotharakos et al. (2004). In the same paper the time evolution of the potential coefficients is shown in figs. 5a,c. They seem to get stabilized fast and stay remarkably constant even for times compared to the Hubble time. The final output gives a triaxial elliptical galaxy. Its ellipticity is about E7 on the Y-Z plane and about E5 on the X-Y plane, in a radius that corresponds to 2 half mass radii (hereafter *hmr*).

Since our aim is to create a system that is rotating around its smallest axis (i.e. the z-axis) we simply rotate the projections of the velocity vectors of all the particles on the X-Y plane to become perpendicular to their position vectors with a counterclockwise sense of rotation, and therefore we give the maximum possible rotation on this plane. This mechanism has already been used in Voglis et al. (2006). Then we let the system evolve using the c-t code again, for another 250 dynamical times and calculate the "spin parameter" λ (Peebles, 1969) as a function of the radius. The spin parameter is calculated by the following formula:

$$\lambda = \frac{J|E|^{1/2}}{GM^{5/2}} \quad (2)$$

where G is the gravitational constant. The angular momentum J , the bounding energy E (in the inertial frame), and the mass M are measured as cumulative quantities along cylinders on the X-Y plane, having the Z-axis as their main axis.

At a time $t = 250t_{units}$ the value of λ has increased dramatically in the inner parts of the barred galaxy and stays close to $\lambda = 0.22$ over most of the extent of the system. This value corresponds to the maximum value of λ for a rotationally supported galaxy and is close to the one of our Galaxy, as it was calculated by Efstathiou & Jones (1979).

In the c-t code we use a new *runit* that corresponds to the limiting radius of the whole bound system i.e. one *runit* is approximately 120 kpc in real units and a new *tunit* that corresponds to the half mass crossing time of the system (hereafter *hmct*). Since a Hubble time is $\approx 300hmct$ (see Kalapotharakos et al. (2004) for details), then $1hmct \approx 45,6Myrs$.

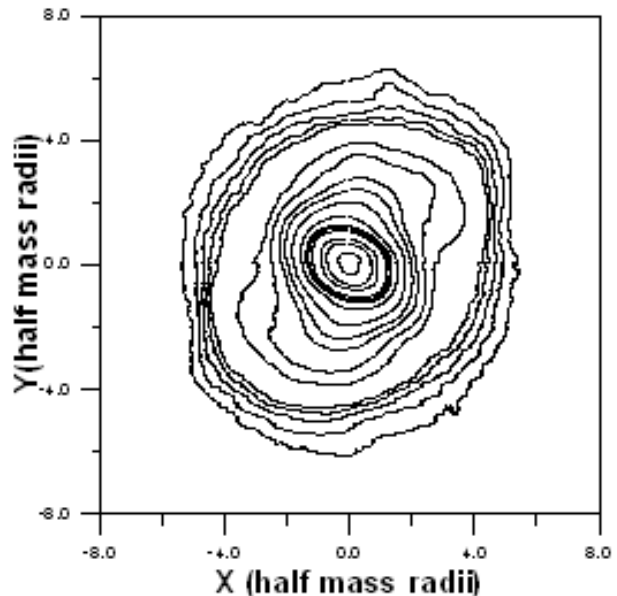


Figure 1. A snapshot of the isodensity contours at time=12hmct

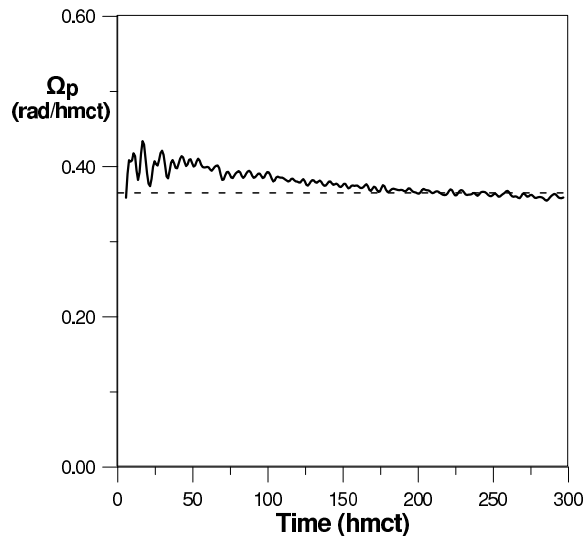


Figure 2. The time evolution of Ω_p of the bar, in radians per half mass crossing time(hmct)

3 CHARACTERISTICS OF THE BAR

In order to calculate the angular velocity of the pattern (hereafter Ω_p) of the system, we must find the time evolution of the angle between the great axis of inertia of the rotating system and a fixed axis, that is the Y-axis of the inertial frame of reference. However, by observing the time evolution of the isodensities on the rotating plane, we notice the existence of a differential rotation of the pattern, i.e. the inner parts seem to rotate faster than the outer parts at the beginning of the c-t run. This lasts up to a certain time, until a single Ω_p is established throughout the radius of the whole configuration. In Fig. 1 a snapshot of the isodensities on the X-Y plane is shown at 12 half mass crossing times (*hmct*) from the beginning of the c-t run. We notice a trailing spiral structure, as the galaxy is rotating as a whole

counterclockwise. This spiral structure seems to travel outwards before it vanishes later on. Therefore angular momentum is transferred to the material outwards. This is a well known mechanism that makes the bar grow stronger and slow down (Lynden-Bell and Kalnajs, 1972). These authors have shown that density waves in the form of temporary spiral structures carry angular momentum from the inner parts to the outer parts. This transference is due to the interaction of the bar perturbation of the gravitational field with stars moving in resonant orbits particularly near the ILR and corotation. They also proved that only in trailing spiral structures do the gravity torques carry angular momentum outwards. Later on Tremaine & Weinberg (1984) and Weinberg (1985) extended this analysis showing that angular momentum transference can be considered as a particular type of dynamical friction. N-body simulations have confirmed this evolution scenario of bar-like galaxies (e.g. Athanassoula, 2003).

In the present experiment this spiral structure vanishes after a short transient period of our calculations i.e. at $t \approx 20hmct$. However, in experiments with a larger value of Ω_p these spiral structures can survive even for times comparable to a Hubble time (Voglis et al., 2006).

In Fig. 2 we plot the time evolution of the angular velocity in units of $rad/hmct$ of the material inside $2.0 r_{hm}$. The fluctuation of Ω_p at the beginning of the c-t run is related to the differential rotation of the pattern which transfers angular momentum outwards. This phenomenon creates spiral structures transiently (see Fig. 1) and causes the formation of tidal torques between the differentially rotating parts. Therefore the material inside the bar can temporarily accelerate or decelerate, before the whole system acquires the same Ω_p . The very small fluctuations after this transient time are less than $1^\circ/hmct$. We notice that the material of the bar seems to slow down and stabilize its angular velocity, after $t \approx 150hmct$ to a value of $\Omega_p \approx 21^\circ/hmct$. This value of Ω_p is equivalent to $(2\pi)/(17hmct) = 0.37rad/hmct$ or to $8.25km/(kpc.sec)$ (dashed line in Fig. 2).

In order to study the orbital structure of this bar-like galaxy and the level of chaos we need good statistics and therefore a second multiplication of the particles is necessary. By considering only the bound part of our galaxy (inside the radius $1.0 runit$) we split again each particle into 9 particles arranged in a small cubic grid around the parent particle, while the sum of these children particles conserves again the mass, energy and angular momentum of the parent particle. The new configuration consists now of about 1.1×10^6 particles. We then let the system relax for another 50 half mass crossing times. After a short time period the system reaches again an equilibrium and rotates with the same Ω_p pattern: $\Omega_p = 0.37rad/hmct$ as a whole.

For studying the orbits that support the bar and determine the level of chaos we take a certain snapshot, where the bar is parallel along one of the main axes of the inertial frame of reference on the plane of rotation, freeze the potential of the system and calculate the orbits in the rotating frame of reference.

At 50 *tunits* of the c-t run, after the new multiplication of the particles, the bar of the galaxy has been aligned with the Y-axis of the inertial system of reference. This is obvious in Fig. 3 where we plot the isodensity contours on the X-Y plane.

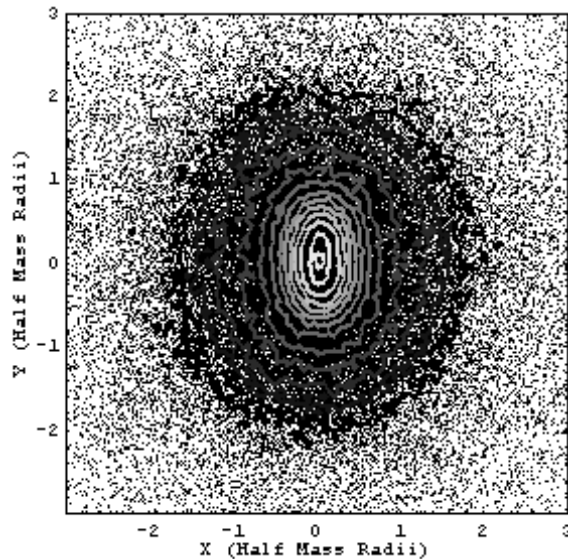


Figure 3. Isodensity contours on the X-Y plane at the end of the N-body run, together with the projections of the real particles of the galaxy.

In Fig. 4 the surface density profile is plotted along the main axis of the bar (black line, Y-axis) and across the main axis of the bar (grey line, X-axis). It is obvious that an exponential-like profile can be fitted (thick line) in the first case almost until the limit of the bar at $\approx 2hmr$, which is a well known property, in the literature, for barred galaxies. The dashed line is the exponential fit of the surface density across the main axis of the bar.

In Fig. 5 we plot the ellipticity $= 1 - b/a$, where a is the semi-major axis and b is the semi-minor axis as a function of the distance along the Y-axis. At this snapshot, the rotating frame of reference coincides with the inertial frame of reference. The calculation has been done using the isodensity contours of Fig. 3. The ellipticity is close to E5 in the inner parts and drops to E1 near the end of the bar, while the isodensities become almost spherical outside corotation.

The boxiness of the isophotes is a well known feature in barred galaxies. This effect can be measured by the shape parameter c , which can be determined from the equation of a generalized ellipse (Athanassoula et al. 1990):

$$(|y|/a)^c + (|z|/b)^c = 1 \quad (3)$$

where a and b are the semi-major and semi-minor axes (calculated from the equidensity contours) and c is the parameter describing the shape of the generalized ellipse. For $c=2$ we obtain a standard ellipse, for $c > 2$ the shape approaches a parallelogram and for $c < 2$ we have a lozenge. In Fig. 6 we plot the shape parameter c as a function of the semi-major axis of each isodensity contour of Fig. 3. From this figure we conclude that in our model, the inner and the outer parts of the bar can be well fitted by ellipses while in a region in between we have somewhat orthogonal-like isophotes. This result agrees with the N-body experiments of Athanassoula & Misiriotis (2002).

An estimate of the perturbation of the bar is the value of $\delta\varrho/\varrho_0$, where ϱ_0 is the mean density and $\delta\varrho$ is the deviation from it along an annulus in a certain distance from the

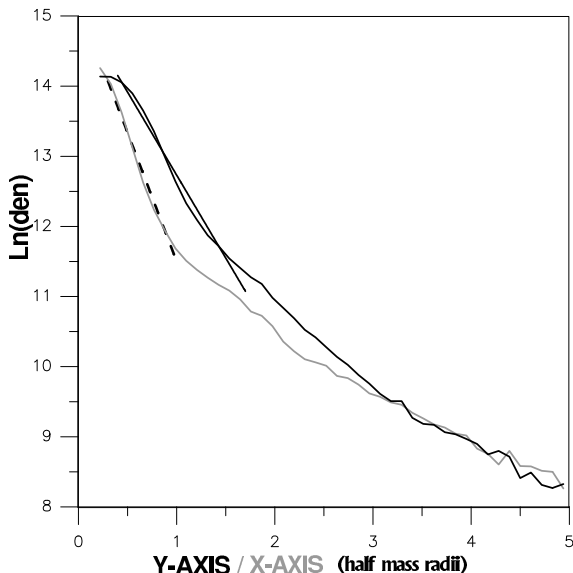


Figure 4. The surface density profile at a time= $250t_{\text{mass}}$ along the Y-axis (black line) and along the X-axis (grey line).

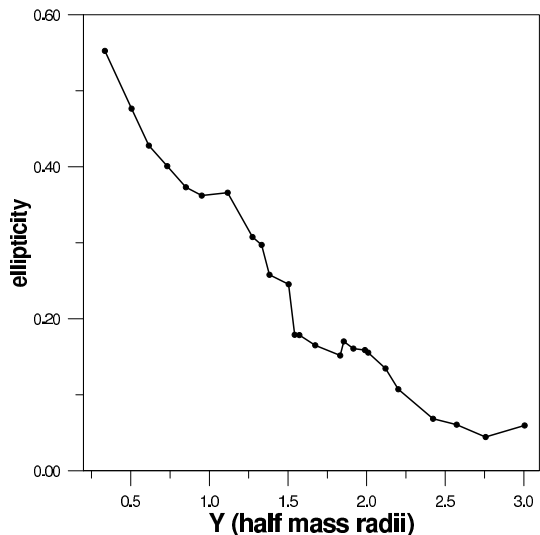


Figure 5. The ellipticity on the X-Y plane as a function of the semi-major axis of the bar.

center. The calculations are made by projecting the particles on the plane of rotation (x-y plane) and dividing the surface into annuli of equal width. Then we also split the xy plane in azimuth (with $d\theta = 2 * \pi / 40$) into 40 successive angles creating bins. Then we count the particles in each bin to calculate the density ρ . We plot the maximum amplitude $\delta\rho/\rho_0 = (\rho - \rho_0)/\rho_0$ in every annulus as a function of y . By changing $d\theta$ from $d\theta = 2 * \pi / 20$ up to $d\theta = 2 * \pi / 50$ we have found optimal values, such that a further decrease of $d\theta$ does not change the maximum amplitudes. In Fig. 7 we present the maximum value of the perturbation of each annulus as a function of the radius. The maxima appear always along the bar (y-axis). We observe that the absolute maximum perturbation is close to 80% and is located a little inside the half mass radius of the system, while the value drops to $\approx 25\%$ near the end of the bar. For the region outside

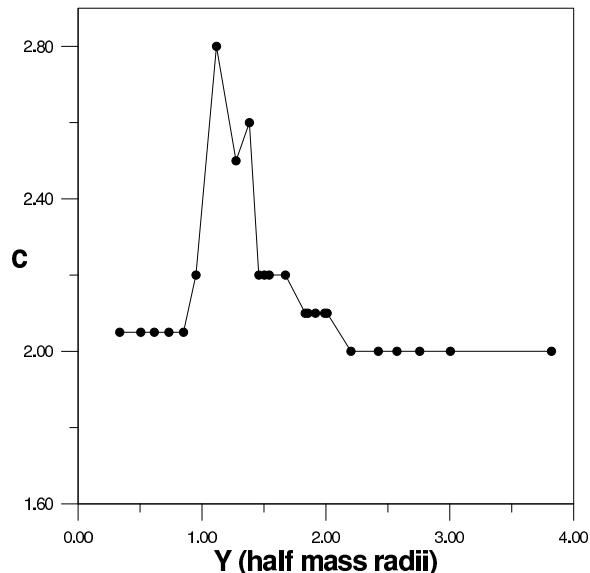


Figure 6. The shape parameter c , as a function of Y (semimajor axis).

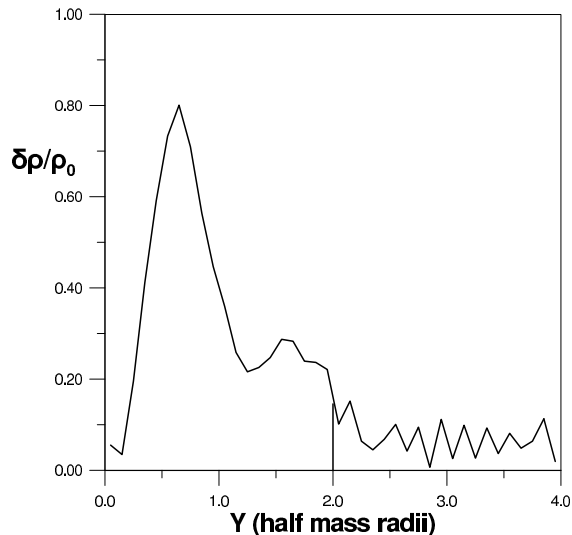


Figure 7. The bar perturbation $\delta\rho/\rho_0$ as a function of y along the bar on the plane of rotation. The end of the bar is at $\approx 2hmr$.

the bar we can only trust the mean value of the saw-tooth part. This perturbation is considered large and is often observed in real barred galaxies. See for example the paper of Laurikainen et al. (2004), where the $m=2$ and $m=4$ components are calculated for a sample of 112 spiral galaxies.

Observers recognise the different components of a barred galaxy by plotting the density profile along and parallel to the the major or minor axis of the bar as it is proposed by Luticke et al. (2000). The bulge length is marked by the increased light distribution over the exponential disk well above the bar. In Fig. 8 we plot the surface density parallel to the minor axis for two different z . For $z=0$ (black line) we see that a central spherical component is present (we also mark the limits of the bar length on the x-axis). For $z=1.6 hmr$ a plateau appears that corresponds to the bar. Therefore we can conclude that this central outcrop corresponds

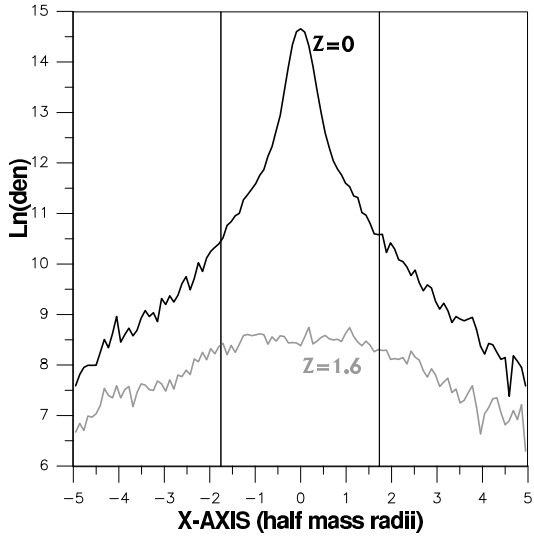


Figure 8. Surface density along the bar minor axis for $z=0$ (black line) and $z=1.6hmr$ (grey line).

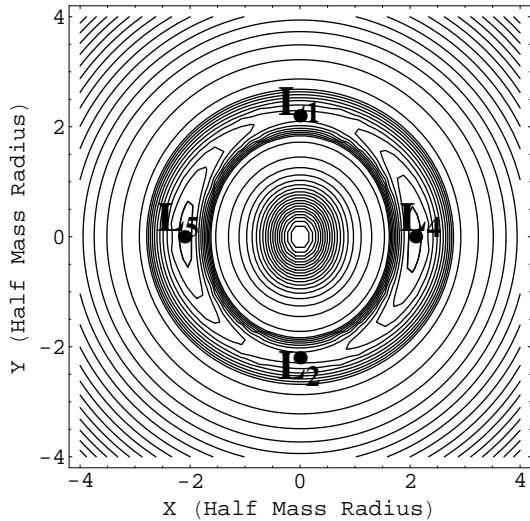


Figure 9. The equipotential contours at the end of our calculations.

to a bulge that has been created self consistently when the system has reached an equilibrium.

Another important quantity for the orbital study is the corotation radius. This can be determined from the maximum value of the effective potential all along the main axis of the bar, as well as from the equipotential contours (Fig. 9) where the L_1 and L_2 points determine approximately the radius of corotation. Therefore we conclude that in our N -body galaxy, corotation is placed at approximately $2.2 hmr$. The Langrangian points L_4 and L_5 are placed at approximately $2.0 hmr$. Figure 9 gives extremely smoothed contours as a result of the program used by "Mathematica".

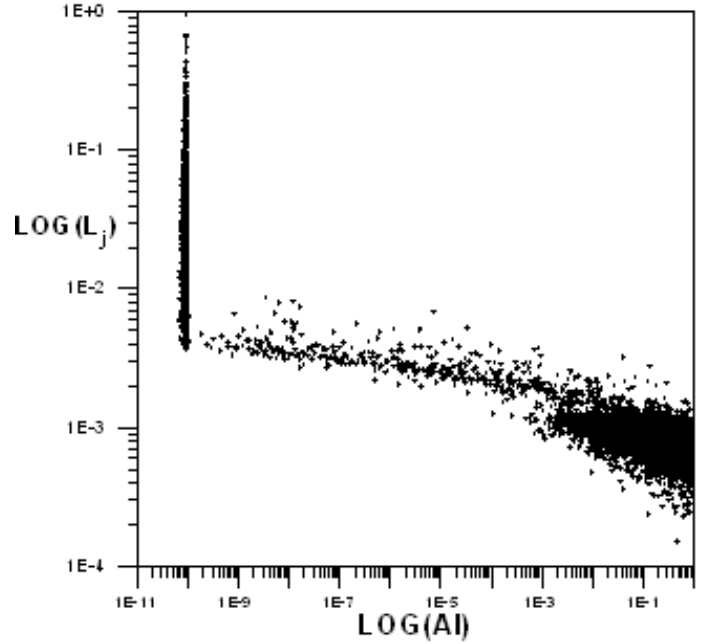


Figure 10. A snapshot of the orbits of the particles in the sample on the plane $\text{Log}(AI) - \text{Log}(L_j)$ at 1200 radial periods.

4 STUDY OF THE LEVEL OF CHAOS

The purpose of this section is to classify the orbits of our self-consistent system in ordered and chaotic ones and find their energy distribution.

This task can be accomplished by using a combination of two methods, that is the Specific Finite Time Lyapunov Characteristic Number (SFTLCN), or simply L_j , and the Smaller Alignment Index, (SALI), or simply Alignment Index (AI)(Skokos 2001, Voglis et al. 2002).

The well known Finite Time Lyapunov Characteristic Number defined by the relation

$$FTLCN = \frac{1}{t} \log \frac{|\xi(\vec{t})|}{|\xi(0)|} \quad (4)$$

is not very suitable for detecting chaotic orbits, because chaos is weak in the present case and the LCN of most of these orbits is small compared with the inverse of the dynamical time of the system; therefore these chaotic orbits cannot be detected by integrating for times equal to only a Hubble time.

This problem can be overcome by using the Specific Finite Time Lyapunov Characteristic Number (*SFTLCN*), or simply L_j for every orbit which is given by the formula:

$$L_j(T_{rj}, t_j) = \frac{T_{rj}}{t_j} \sum_{i=1}^{N_j} a_{ij} \quad (5)$$

where t_j is the integration time, N_j is the number of time steps ($\Delta t = t_j/N_j$) and a_{ij} is the stretching number (Voglis and Contopoulos 1994) at the time step i ($i = 1, \dots, N_j$). The stretching number a_{ij} is defined by the equation

$$a_{ij} = \ln \frac{|\xi_j(t_i + \Delta t)|}{|\xi_j(t_i)|} \quad (6)$$

where $\xi_j(t_i)$ is the length of the deviation vector from the

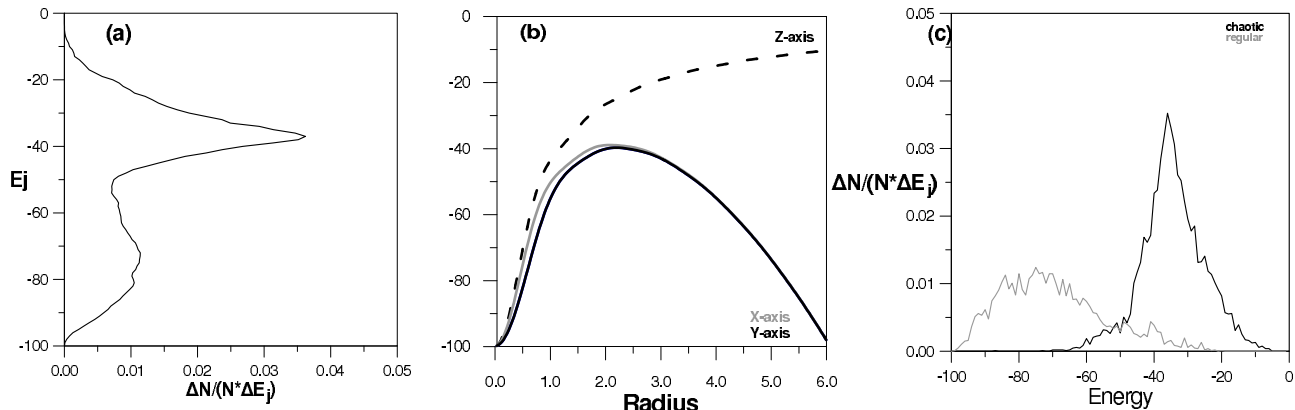


Figure 11. (a) The energy distribution of the total number of particles. (b) The effective potential along the X,Y and Z axes. (c) The energy distribution of particles having chaotic orbits(black line) and of particles having regular orbits(grey line).

orbit j at time $t = t_i$. To avoid numerical overflows the deviation vectors are normalized to unity at regular time steps. The equations giving the deviation vectors are linear and therefore a change of their measure by a constant does not affect the information we get. The time evolution of the deviation vectors is found from the variational equations of motion. The coefficients of these equations are evaluated numerically. The quantity T_{rj} is the average radial period of the orbit of the particle j , i.e.the time that a star needs to go from its pericenter to its apocenter and back. This period scales with the energy E_j of the orbit as $T_{rj} \approx |E_j|^{-3/2}$ almost independently of the angular momentum (Voglis 1994).

The above definition of the SFTLCN allows us to extend our calculations to different times for every orbit, up to a point when the integration time is long enough to allow LCNs to be stabilized at constant small values.

In the second method (using AI), we use the properties of the time evolution of the deviation vectors (Voglis et al. 1998, 1999).

In particular, we consider the time evolution of two arbitrary different initial deviation vectors ξ_{j1} and ξ_{j2} of the same orbit. If the orbit is chaotic, then the smallest of the two norms $d_{j-}(t) = |\vec{\xi}_{j1}(t) - \vec{\xi}_{j2}(t)|$ and $d_{j+}(t) = |\vec{\xi}_{j1}(t) + \vec{\xi}_{j2}(t)|$ is called Alignment Index (AI) and tends exponentially to zero. However, in our calculations we impose a cutoff limit e.g. $AI = 10^{-10}$ to save integration time. On the other hand, if the orbit is ordered, then d_{j-} or d_{j+} oscillate around a roughly constant mean value. This value is usually close to unity and in any case it is not less than 10^{-3} .

Thus, by following the evolution of the smaller of the two indices d_{j-} , d_{j+} , we can distinguish between regular and chaotic orbits.

We adopt a value for the Hubble time, equal to 100 half mass crossing times T_{hmct} of the system. We usually calculate the L_j s and AI of ordered orbits for the same number of radial periods, namely $t_j/T_{rj} = 1200$. However, in the case of the chaotic orbits the integration time varies due to the cutoff limit imposed.

The comparison of the two methods mentioned above can be shown in Fig. 10. The sharp line on the left part of the figure (at $AI=10^{-10}$) represents the most chaotic orbits and it is due to the cutoff limit. The triangular distribution

on the lower right part of the figure represents the ordered orbits. Finally, the lane of points between these two regions represents orbits that are weakly chaotic.

Almost 60% of the orbits were found chaotic. This percentage is higher than the percentage of chaotic orbits in non rotating systems, representing elliptical galaxies, which is near 30% at most (see for example Voglis et al. 2002). Furthermore, the Lyapunov characteristic numbers of the chaotic orbits are larger by about one order of magnitude than in the non-rotating self-consistent systems, a result that is related to the resonance effects near corotation. However only the 35% of the total mass can eventually develop chaotic diffusion in a Hubble time (Voglis et al. 2006).

In Fig. 11 we plot the energy distribution of the particles at the end of our calculations, that is after 250 half mass crossing times T_{hmct} of the system. Figure 11a shows the distribution of the total number of particles, where $\Delta E_j = 1$ (in our units which are normalized to -100 at the potential well) and represents the amplitude of the energy bin. The distribution presents two peaks. Figure 11b shows the effective potential along the X,Y and Z axes in half mass radius units (rh_m) and Fig. 11c shows the energy distribution of chaotic orbits alone (black line) and ordered orbits (gray line). By comparing these figures we conclude that the sharpest peak of the distribution of the particles corresponds mostly to chaotic orbits (since there are almost no regular orbits there). This peak is located at $E_j \approx -36$, around corotation, as expected, and corresponds to a radius $\approx 2.2rh_m$. The second peak is located at $E_j \approx -75$, is related exclusively to regular orbits.

5 STUDY OF THE ORBITAL STRUCTURE

The purpose of this section is to classify the orbits of our self-consistent system in such a way as to determine the shape and the percentage of the orbits that support the bar. For this purpose we have used two powerful tools: a) the surface of section for test particles as well as for real N-body particles and b) the frequency analysis of the real N-body orbits.

5.1 Surface of section

We fix the values of the coefficients of the analytical expansion of the potential and construct surfaces of section (SOS) for different energies E_j in the rotating frame (Jacobi constants):

$$E_j = \frac{1}{2}(v_x^2 + v_y^2 + v_z^2) + V(x, y, z) - \frac{1}{2}\Omega_p^2 R_{xy}^2 \quad (7)$$

where $V(x,y,z)$ is the frozen potential of both the axisymmetric part and the bar perturbation, given by the N-body run, v_x, v_y, v_z are the velocities in the rotating frame of reference and Ω_p is the angular velocity of the bar rotating as a solid body and calculated as in Fig. 3.

We first use test particles for constructing SOS. In our 3-D model the SOS are 4D and we plot their projections on the x, \dot{x} plane, for $y = 0, \dot{y} > 0$ and having initially $z = 0$ and $\dot{z} = 0$. All sections are made in the rotating frame of reference. A similar technique has been used by Contopoulos et al. (2002) and Kalapotharakos et al. (2004) in order to examine the phase space structure and the foliation of the invariant tori of the orbits due to the third integral in non-rotating triaxial self-consistent systems.

The values of x are normalized with the half mass radius (hmr). The Lagrangian points L_1, L_2 (and therefore the corotation radius) are located at $\approx 2.2hmr$.

In Fig. 12 we plot the SOS which corresponds to a Jacobi constant $E_j = -39$. All values of the Jacobi constant are normalized so that the well of the potential corresponds to -100. All the initial conditions in Fig. 12 have been chosen along $\dot{x}=0$ and they have been integrated for 200 iterations each. Figure 12a presents the region outside corotation where a few stable orbits around L_5 are present. Most of the orbits of this figure reach large distances and a part of them escape. Figure 12b presents the region inside corotation. Some important resonances are marked, i.e. the 3:1, 4:1 and 5:1 resonances (that appear near the end of the bar), as well as the "x4" type orbit (Contopoulos and Papayanopoulos 1980) which has a main axis perpendicular to the bar and is retrograde with regard to the sign of Ω_p . In Fig. 13 the corresponding periodic orbits are plotted. Every periodic orbit intersects the SOS at one or a finite number of points. The stable periodic orbits are easily identified on the SOS, because they are surrounded by closed invariant curves.

In Fig. 14 we have plotted the real particles from the N-body run. We have chosen the initial conditions of particles having a Jacobi constant equal to $E_j = -39 \pm 0.5$ and we have integrated them in a fixed potential for 100 iterations. In this energy level only a small fraction of the orbits of real particles are regular as it can be seen from Fig. 11c. Figures 12a and 14a present the region outside corotation containing test particles and real N-body orbits respectively around the L_5 point. We see several thick dark lines that are called "rays". An explanation of the ray structure of this figure was given by Contopoulos & Patsis (2006) who noticed that even in the chaotic region we may see a structure of rays (see Fig. 9 of Contopoulos & Patsis (2006)). The successive iterates of every initial point along a ray are located also on rays, and they move in a clockwise way around the center of the black region. After each return the points deviate from their initial positions and therefore the rays thicken in time and finally they join each other. Thus the ray structure

disappears if we take a much greater number of iterations than in Fig. 14a.

Figure 14b presents the region inside corotation. It is obvious that the area corresponding to the "x4" orbits is depopulated while the orbits supporting the shape of the bar and having the same sense of rotation with it, are well populated.

In Fig. 15 the surface of section for test particles is plotted for another value of the Jacobi constant $E_j = -42$. Figure 15a presents the region outside corotation. It is remarkable that some islands of stability exist that correspond to the OLR and -1:1 resonances. Their corresponding orbits are shown in Fig. 15c. For the area inside corotation (Fig. 15b) the stable orbits correspond to the 3:1, 4:1 and 5:2 resonances, as well as to the "x1" type of orbits with loops at the edges and the retrograde "x4". In Fig. 15d the corresponding orbits are plotted.

The same surface of section for the real N-body particles is shown in Fig. 16. The main resonances supporting the bar are populated here again while the area around the "x4" orbit is depopulated. Another important remark is that real particles avoid the area of the OLR as well as the -1:1 resonance outside corotation. A remarkable feature common for test particles as well as for real N-body particles is the intensely dark area around the OLR and -1:1 resonances in the region outside corotation. (compare Figs. 14a and 16a). This is an indication of the existence of a cantorus which impedes the communication of the two chaotic regions, imposing a partial barrier in this 2-D projection of the section. On the other hand since our N-body system is 3-dimensional, one would expect that Arnold diffusion would transport particles through the third dimension and produce a communication between the two chaotic regions (for a definition of Arnold diffusion see Contopoulos 2002). However, our results indicate that such a communication is very slow, therefore Arnold diffusion is not efficient. In Fig. 17 the SOS is plotted for test particles, with $E_j = -46$ for the region outside corotation (Fig. 17a) and for the region inside corotation (Fig. 17b). Figure 17c shows the 2-D approximation of the SOS when there is no third dimension, i.e. the forces on the z-axis are exactly zero. In this figure we mark some important tori. Every torus is characterized by its rotation number, i.e. the average angle between successive intersections of an orbit by the SOS, as seen from a central fixed point. This number can be represented in the form of a continued fraction:

$$[\alpha_0, \alpha_1, \dots] \equiv \frac{1}{\alpha_0 + \frac{1}{\alpha_1 + \dots}} \quad (8)$$

If $\alpha_i = 1$ for all i beyond a certain j , this number is called a noble number.

In the region outside corotation the existence of different tori and cantori separates the different chaotic regions. By comparing Fig. 17c with Fig. 17a we see only minor differences. In Fig. 17c the chaotic region inside the torus [1,1,1,7,1,1,..] is united but it is obvious that a cantorus still exists separating the two unequally darkened areas (a cantorus is a torus with a Cantor set of holes). We have taken an initial condition in the most darkened area of this SOS, between [1,1,1,7,1,1,..] and [1,2,3,1,1,..] and we have seen that the orbit stays located there for at least 5×10^5 iterations and possibly for ever. Therefore we conclude that there may still

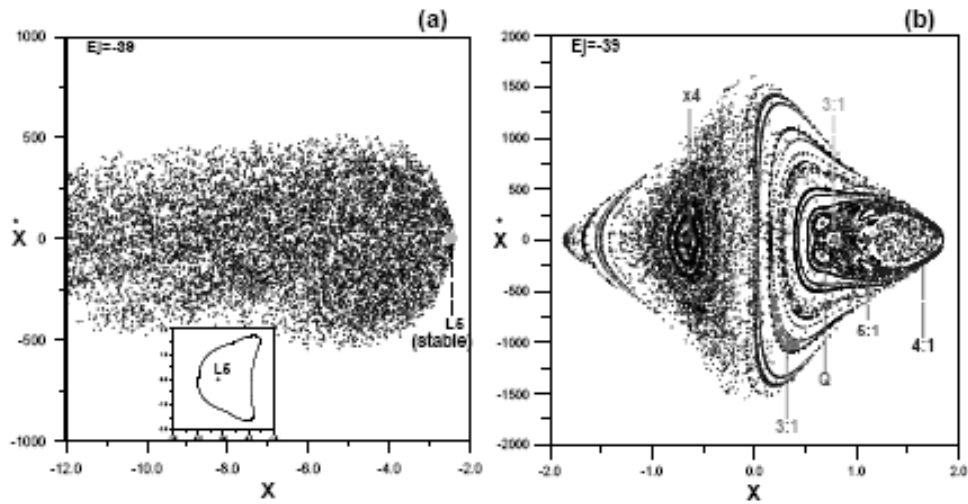


Figure 12. (a) The surface of section of test particles with a value of the Jacobi constant equal to -39 for the region outside corotation. The insert box gives the stable periodic orbit around L5 point. (b) The same for the region inside corotation.

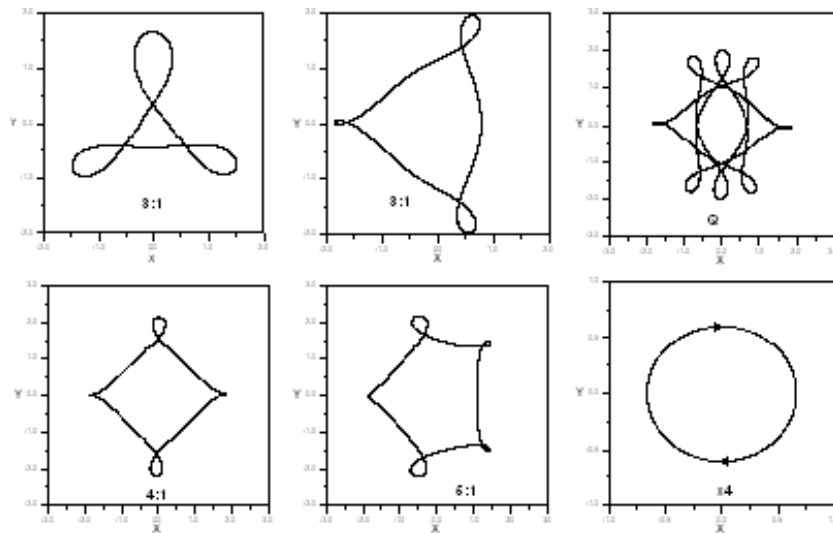


Figure 13. Periodic orbits that intersect the SOS at the points indicated in Fig. 12(b).

exist tori (or cantori with very small holes) corresponding to a noble number [1,1,1,7,1,1,...] that puts an inside barrier and to [1,2,3,1,1,...] that puts an outside barrier for this chaotic area.

The same phenomenon is obvious in Fig. 18 where the same projection of SOS is plotted for real N-body particles for the region outside corotation (a) and for the region inside corotation (b). Here again it is obvious that for the region outside corotation, the real orbits (that are chaotic in their majority) are restricted in areas that are bounded by the same tori, while there are areas with almost no N-body particles at all. Therefore tori and cantori on the projection of the SOS, play an important role in retaining chaotic orbits projected on the 2-D space of the galaxy, limiting the effectiveness of Arnold diffusion through the third dimension.

The range of energies for which there exist cantori as described above is $-60 < E_j < -45$. In this range the amounts of ordered and chaotic orbits are of the same order (see Fig. 11c).

There are two mechanisms that force chaotic orbits to stay bound inside specific areas and make them dynamically important for the system. The first one, that has been described above, is the phenomenon of cantori that put a partial barrier on the SOS and reduce the effectiveness of Arnold diffusion. The second one is the stickiness effect of a fraction of the chaotic orbits near resonances that support the bar. Stickiness appears in systems of 2 or more degrees of freedom when chaotic orbits remain close to an invariant manifold for long times before escaping to large distances. This phenomenon is described in the book of Contopoulos

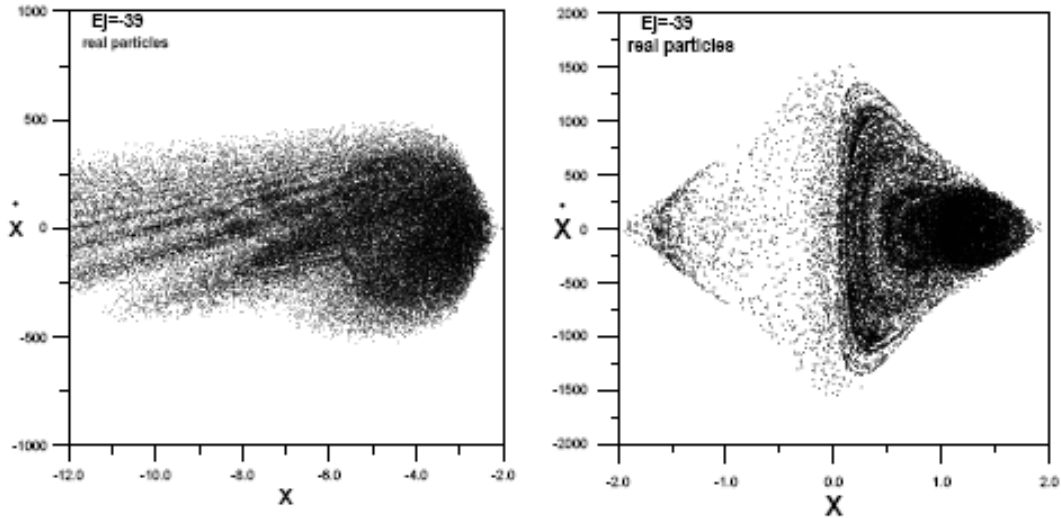


Figure 14. The surface of section of real N -body particles with a value of the Jacobi constant equal to -39 : (a) for the region outside corotation and (b) for the region inside corotation.

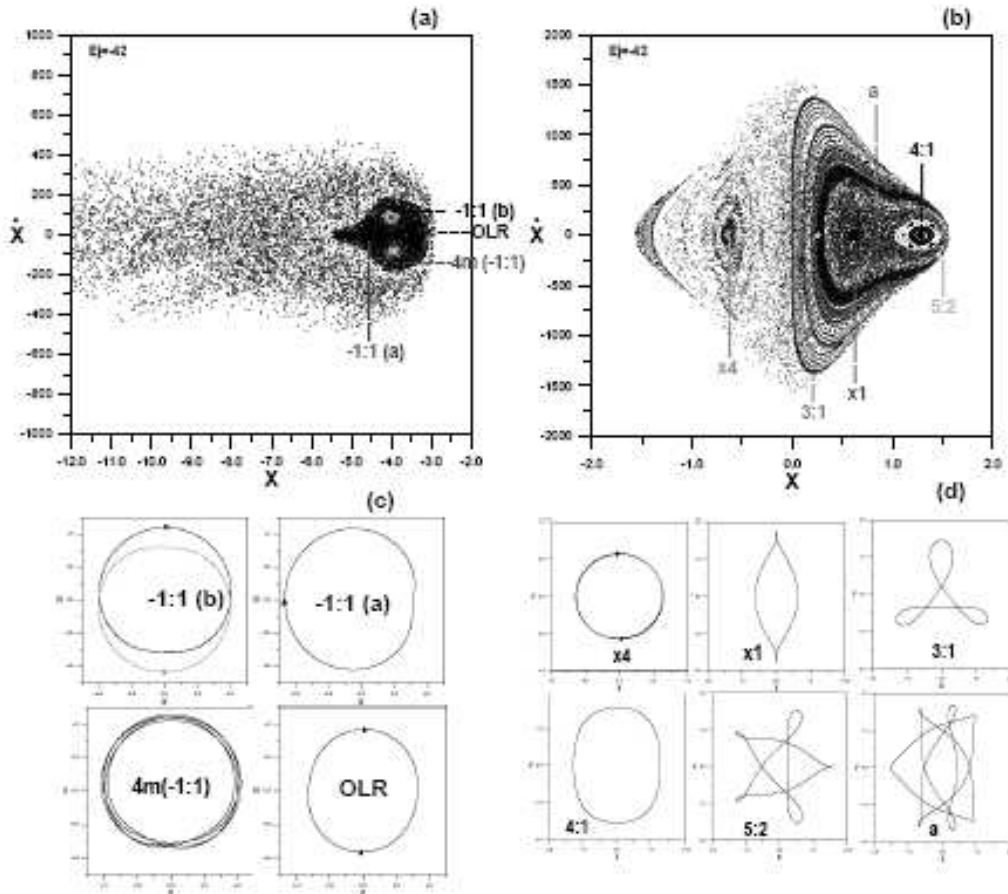


Figure 15. The surface of section of test particles with a value of the Jacobi constant equal to -42 : (a) for the region outside corotation and (b) for the region inside corotation. (c) Orbits corresponding to the region outside corotation: There are two orbits $-1:1$ (b)) and a multiplicity 4 orbit that has bifurcated from $-1:1$ (b). (d) Orbits corresponding to the region inside corotation.

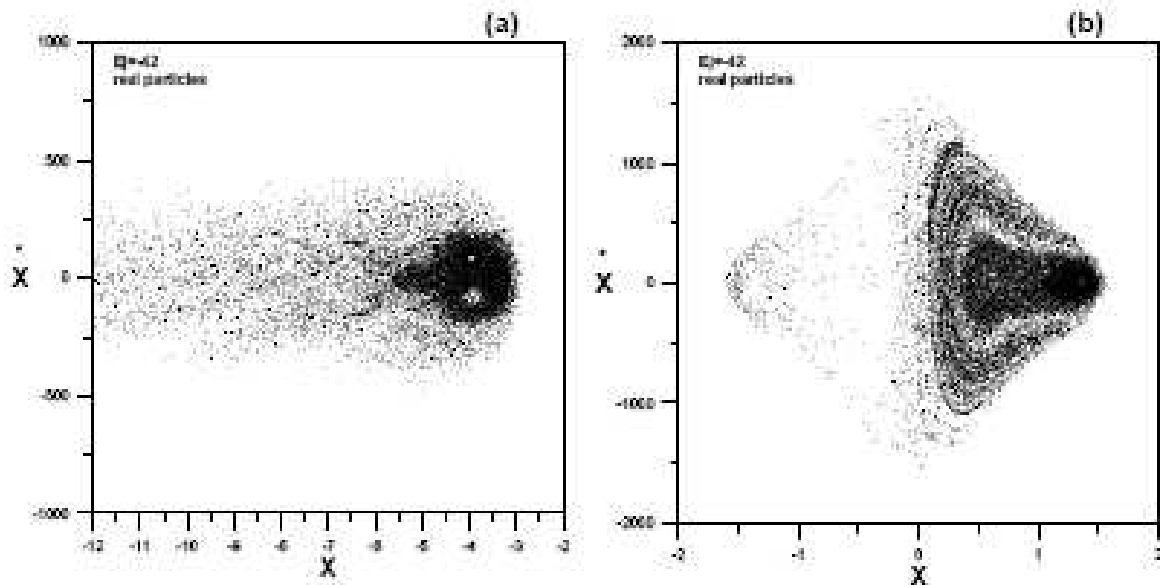


Figure 16. Same as in Figure 15a,b but for the real N-body particles: (a) for the region outside corotation and (b) for the region inside corotation.

(2002). This can be shown from the frequency analysis in the next section. The latter mechanism makes the role of the chaotic layer near the limits of the bar important in supporting its ellipticity and boxiness.

In Fig. 19 we plot the orbits corresponding to islands of stability for the region inside corotation of Fig. 17b. The rotation number is the average frequency of rotation around a fixed point of a stable periodic orbit (here OLR) on the phase space. The rotation number as a function of x along the thick line shown in Fig. 17a is plotted in Fig. 20. In this figure we mark several islands of stability with rational rotation numbers and the noble numbers of some important cantori. We note that the number of islands is smaller than in the case of Contopoulos & Patsis (2006). This is due to the fact that the bar perturbation is larger for the corresponding Jacobi constant in the present model, thus chaos is stronger.

5.2 Frequency analysis of the orbits

In Fig. 21 we plot the main frequencies of all the regular orbits out of a sample of 10764 particles at the end of the N-body run in polar coordinates. We have used time series for each orbit that correspond to a time interval of 100 radial periods. The abscissa corresponds to the frequency of the variation of the radius of the orbit on the plane of rotation (x - y plane in the rotating frame of reference) and the ordinate corresponds to the frequency of the angle φ between the position vector on the plane of rotation and the main axis of the bar (y axis in the rotating frame of reference). Both frequencies are regularized by the frequency in the third dimension (z -axis). It is obvious from this figure that there are groups of orbits concentrated all along lines of specific resonances and others that are more scattered in

between the lines of resonances. Moreover along the same line there can be different groups of orbits belonging to the same resonance. For example on the 2:1 line there are three groups of orbits: the "x1" type with the main axis along the axis of the bar, the "x4" type (only a very small fraction of the total sample) with the main axis perpendicular to the main axis of the bar, and the 2:1 orbits near corotation (n.c) that have a more rectangular shape.

In Fig. 22 we plot the three projections of some real N-body orbits that correspond to different resonances. From this figure it is obvious that in the majority of the orbits that are near resonances the third dimension is not of great importance and the projections on the plane of rotation have shapes that support the bar. We denote as "box" the orbits that are found scattered in between the resonances. In particular we see some groups of orbits that are concentrated in rather small areas in Fig. 21, like Group A and Group B. Group A has orbits that support the bar. Orbits of this type near the limit of the bar are boxy in shape. On the other hand Group B orbits are more spherical on the plane of rotation and their projections on the other planes have a considerable thickness.

Figure 23 is the same as Fig. 21 but for the chaotic orbits of our self-consistent system. The orbits are calculated here up to 300 radial periods. The distribution is more scattered on this figure, as expected. However we can still identify concentrations around resonances. This is a consequence of the fact that most of these orbits are only weakly chaotic.

In Fig. 24 we plot the projections of some real N-body chaotic orbits that have frequencies near resonances. On the xy -plane (of the rotating frame of reference) we have plotted the orbits for 100 radial periods as well as for 300 radial

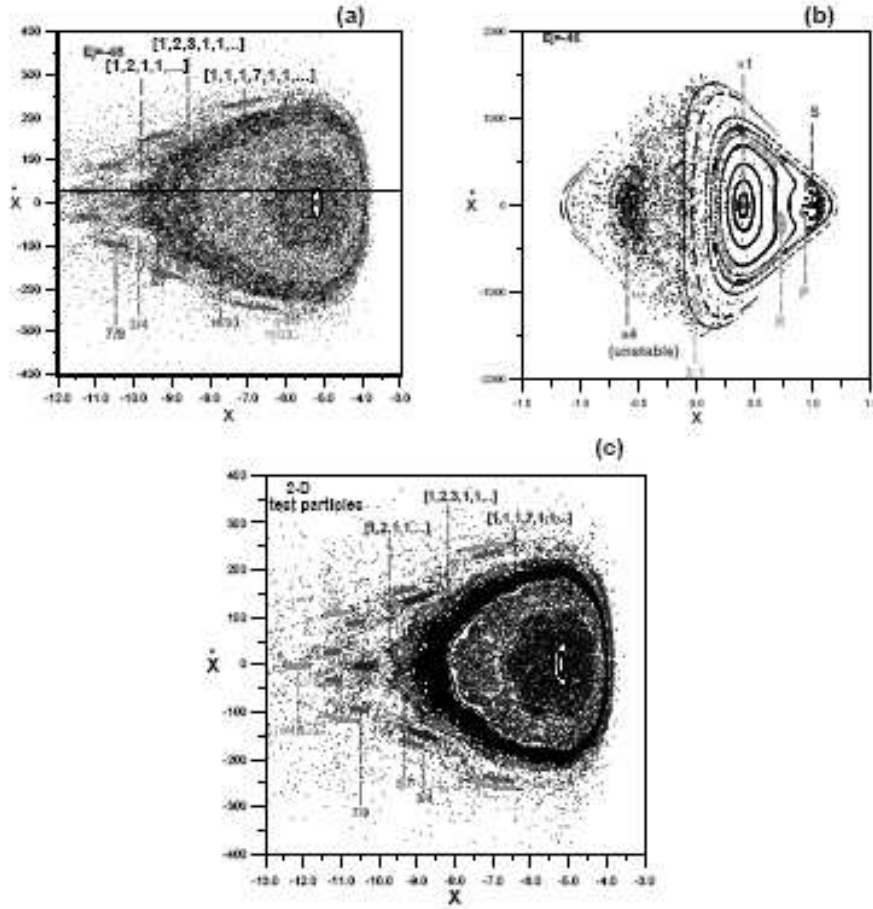


Figure 17. SOS for $E_j = -46$: (a) for test particles for the region outside corotation and (b) for the region inside corotation. (c) SOS for the 2-D approximation of the region outside corotation.

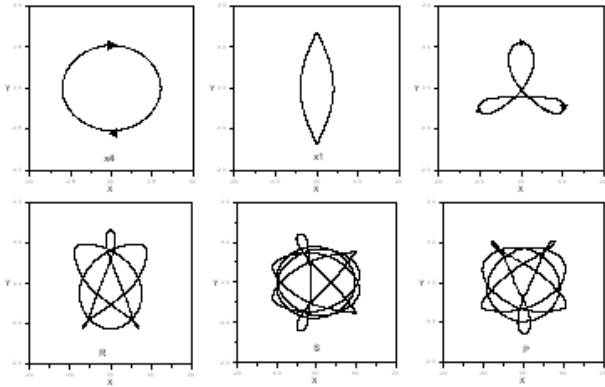


Figure 19. Orbits corresponding to the SOS of Fig. 17b.

periods. We see that orbits do not change considerably from 100 to 300 periods.

Group A corresponds to orbits with a boxy shape and can be found near the end of the bar as well as in smaller radii. Group B corresponds to orbits more spherical and in general with their main axis perpendicular to the bar with

an important thickness in the 3rd direction (z -axis). Most of these orbits present a "X-shape" on the zx plane.

We have also found some families of 3-D orbits whose projections on the rotating plane support the bar and have been found and named in 3-D models by Skokos et al. (2002). In Fig. 24 there are examples of real N -body chaotic orbits with boxy shape that support the bar all along its radius, like for example the 2:1 and 4:1 resonant orbits or the orbits of group A. Similar orbits are found in models of barred galaxies by Patsis et al. (1997). The spatial distribution of the chaotic orbits is in general more spherical than the one of the regular orbits, i.e. the shape of the bar is supported mostly by the regular orbits (Voglis et al. 2006). However there is a layer of weakly chaotic orbits that belong mostly to the outer part of the bar and support the shape of the bar.

In Fig. 25 we show the statistics of the resonances for regular (gray) as well as for chaotic orbits (black). We take a width ± 0.02 around each resonance to populate the orbits. We find that 20% of the chaotic orbits lie near resonances and only orbits of this percentage are plotted in Fig. 24.

In Voglis et al. (2006) the authors have found for this

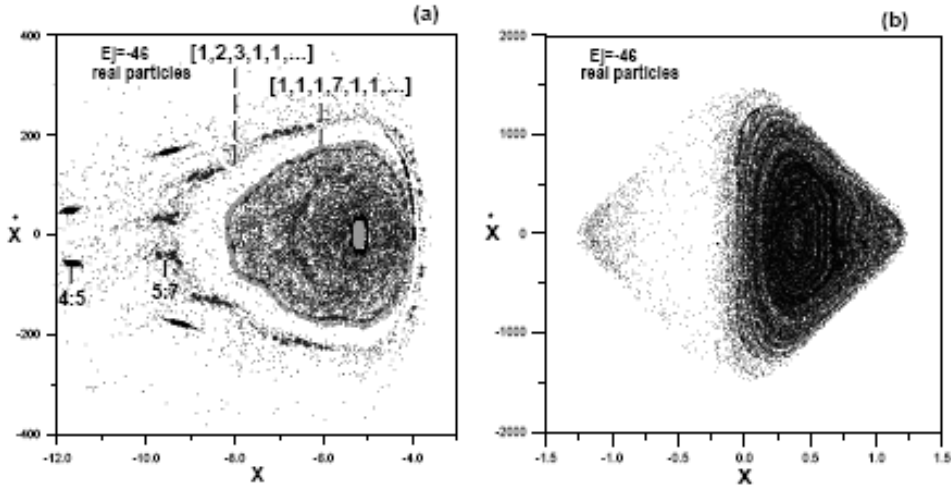


Figure 18. Same as in Fig. 17a,b for the real N-body particles.

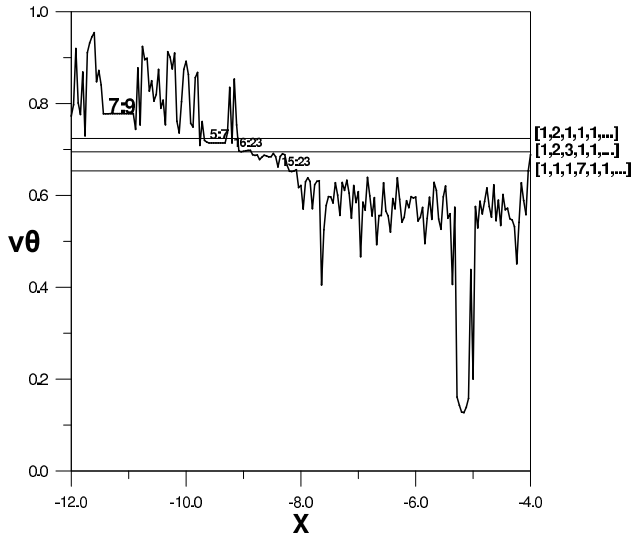


Figure 20. The rotation number as a function of x along the thick line shown in Fig. 17a.

experiment (named QR1) that although 60% of the total matter is chaotic, only a fraction of 35% of the total matter can develop chaotic diffusion in a Hubble time. Therefore the rest 25% of the total matter is weakly chaotic and is mostly located in a layer at the edge of the bar in resonant form, or in regions outside corotation limited by certain tori and cantori (see Figs. 16,17).

6 CONCLUSIONS

We have studied the orbital structure of rotating self-consistent bar-like N-body equilibrium systems. The amplitude of the bar is relatively large ($\delta\rho/\rho_0$ is about 80%, maximum). The angular velocity of rotation of the pattern

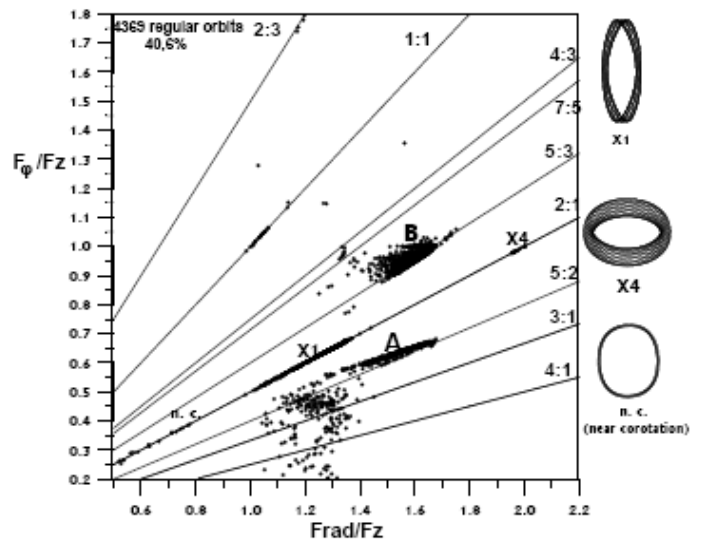


Figure 21. Frequency analysis for the regular orbits.

is $\Omega_p = (2\pi)/(17hmct) = 0.37 \text{ rad}/hmct$, which is equivalent to $8.25 \text{ km}/(\text{kpc}\cdot\text{sec})$, the spin parameter being roughly that of our Galaxy.

The main conclusions of our study are the following:

1) In our N-body experiment that simulates a rotating barred galaxy, chaos is very appreciable, amounting to about 60% of the total bound matter in contrast with nonrotating systems, which have $\approx 30\%$ chaos. However chaos is in general weak and only about 35% of the mass develops chaotic diffusion in a Hubble time.

2) The ellipticity of the bar decreases outwards from 0.5 (E5 galaxy) in the inner parts to about 0.1 (E1 galaxy) in the outer parts.

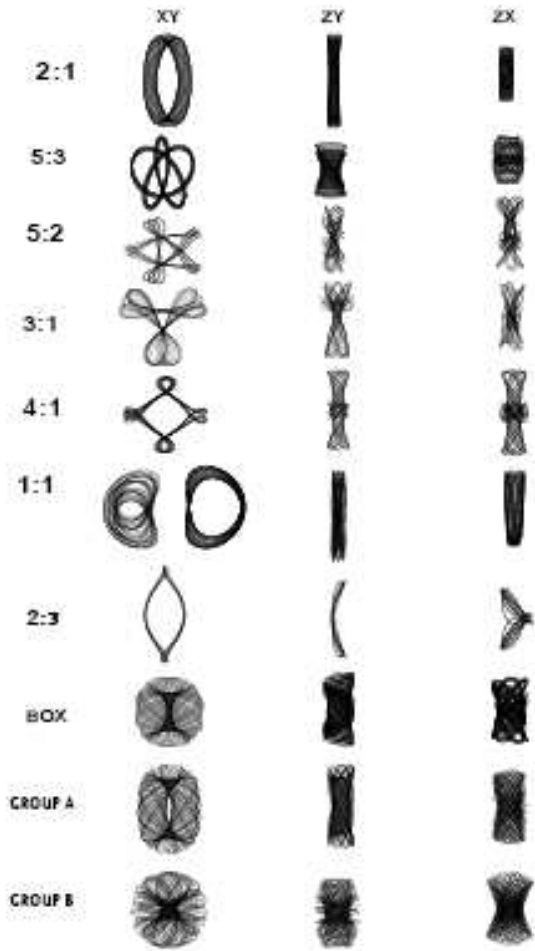


Figure 22. Some examples of real *N*-body regular orbits.

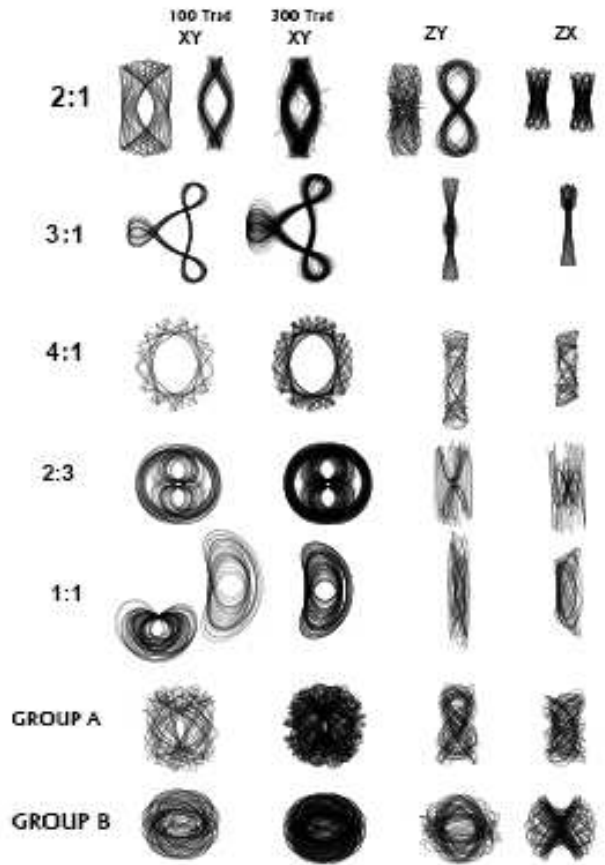


Figure 24. Some examples of real *N*-body chaotic orbits.

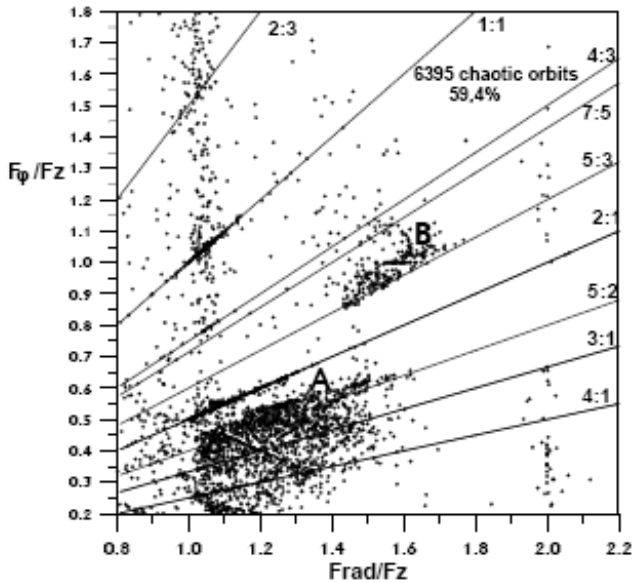


Figure 23. Frequency analysis for the chaotic orbits.

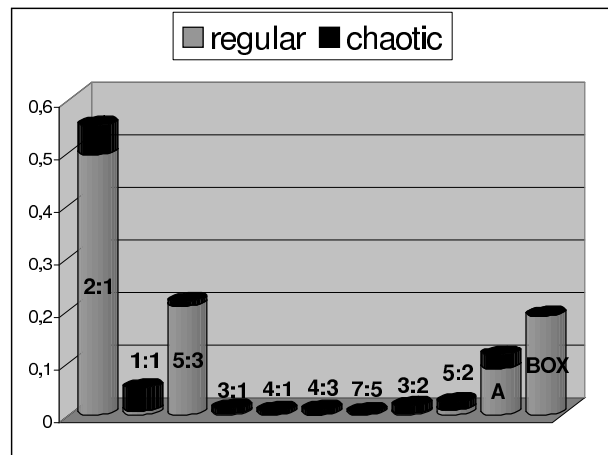


Figure 25. The statistics of the regular and chaotic orbits.

3) The bar is like an orthogonal parallelepiped with a boxiness parameter that is maximum in the middle of the bar.

4) Only weak spirals appear in the present model, and they vanish relatively fast.

5) A comparison is made between systems of test particles and *N*-body systems by projecting the orbits on a 2-D surface of section (SOS). We notice, first, that in both cases

chaos is dominant outside corotation, while most orbits in the bar are ordered.

6) In the outer regions of the SOS of test particles as well as of real N-body particles, we see some thick dark "rays". The particles of these rays have their images along other rays, but after longer times these images fill the regions between the rays, and the rays disappear.

7) Certain outer regions of the SOS have different degrees of darkness in the case of test particles. These regions are separated by invariant tori or cantori. The invariant tori do not allow any communication across them in the 2-D case. In the 3-D case we see similar results although communication is in principle possible by means of Arnold diffusion. Thus Arnold diffusion is probably not effective in the present case. On the other hand cantori allow communication across them but this process is slow if the cantori have small holes, and for a long time the areas from both sides of these cantori do not communicate.

8) The regions inside corotation on the SOS contain mostly ordered orbits. However there are important differences between the test particles case and the N-body case. In particular real orbits do not follow retrograde orbits around x_4 . In general N-body orbits do not enter the regions of islands if they were not inside such islands originally.

9) We have found the forms of the periodic (planar) orbits and the rotation numbers along a particular straight line on the surface of section that allows to locate the small islands and the positions of tori and cantori. These tori and cantori have noble rotation numbers, i.e. their expansions in continued fractions end with an infinity of 1s.

10) A frequency analysis of ordered orbits has identified clearly the various resonant forms of nonperiodic orbits that form islands of stability. We found also stable orbits of box type outside the islands.

11) We did also a frequency analysis of chaotic orbits. The frequency diagram has several similarities with the corresponding diagram for regular orbits, although it is more diffuse. This is due to the fact that chaos is rather weak in the present case.

12) Finally we give the statistics of the various types of ordered and chaotic orbits. The most important orbits are the x_1 orbits, of 2:1 type. These orbits support the bar. But other orbits, like the box orbits and the orbits of group A also support the bar. In particular the group A orbits are mainly responsible for the boxiness of the bar. A 20% of the chaotic population are located near resonances and play an important role in supporting the boxiness of the bar in its outer layers. On the other hand there is also a percentage of chaotic orbits that are located in restricted areas outside corotation limited by tori and cantori in the 2-D projections of SOS. The effectiveness of Arnold diffusion around these tori and cantori is restricted.

In a future paper experiments with stronger and longer lived spiral arms will be presented.

ACKNOWLEDGMENTS

We would like to thank Dr. P. Patsis and Dr. C. Kalapotharakos for fruitful discussions.

REFERENCES

- Allen A. J., Palmer P. L. and Papaloizou J.: 1990, *MNRAS*, 242, 576.
- Athanassoula E., Morin S., Wozniak H., Puy D., Pierce M., Lombard J. and Bosma A.: 1990, *MNRAS*, 245,130.
- Athanassoula E. and Misiriotis A.: 2002, *MNRAS*, 330, 35.
- Athanassoula E.: 2003, in "Galaxies and Chaos", eds. G. Contopoulos and N. Voglis, Springer, 313.
- Barnes E. and Tohline E.: 2001, *Ap.J.*,551 p.80.
- Ceverino D. and Klypin A.: 2005, in *astro.ph 3710c*.
- Contopoulos G., "Order and Chaos in Dynamical Astronomy", Springer, 2002.
- Contopoulos G. and Grosbol P.: 1989, *Astron. Astrophys.*, 1, 261.
- Contopoulos G. and Papayanopoulos: 1980, *Astron. Astrophys.*, 92, 33.
- Contopoulos G. and Patsis P.A.: 2006, *MNRAS*, 369, 1039.
- Contopoulos G., Voglis N. and Kalapotharakos C.: 2002, *Cel. Mech. Dyn. Astr.*, 83, 191.
- Davis M., Efstathiou G., Frenk C. S. and White S. D. M.: 1985, *ApJ.*, 292, 371.
- Efstathiou G. and Jones B.J.T.: 1979, *MNRAS*, 186, 133.
- Hernquist L.: 1988, *Comput. Phys. Commun.*, 48, 443.
- Kalapotharakos C., Voglis N. and Contopoulos G.: 2004, *Astron. Astrophys.*, 428, 905.
- Laurikainen E., Salo H., Buta R. and Vasylyev S.: 2004, *MNRAS*, 355, 1251.
- Lutticke R., Dettmar R.J. and Pohlen M.: 2000, *Astron.Astrophys.*, 362, 435.
- Lynden-Bell D. and Kalnajs A. J.: 1972, *MNRAS.*, 157, 1.
- Miwa T. and Noguchi M.: 1998, *Ap.J.*, 499, p.149.
- Patsis P.A., Athanassoula E. and Quillen A.C.: 1997, *Astroph. J.*, 483, 731.
- Peebles P.J.E.: 1969, *Astroph. J.*, 155, 393.
- Shen J. and Sellwood A.: 2004, *Ap.J.*, 604, p.614.
- Sundin M.: 1996, "Barred Galaxies", ASP Conference Series, eds. Buta R., Crocker R. M. and Elmegreen B., 921 p.423.
- Sundin M., Donner K.J. and Sundelius B.: 1993, *Astron. Astrophys.*, 280, 105.
- Skokos Ch.:2001, *J. Phys. A: Math.Gen.*, 34, 10029.
- Skokos Ch., Patsis P.A. and Athanassoula E.:2002, *MNRAS*, 333,847.
- Sparke L. and Sellwood J.A.: 1987, *MNRAS*, 225, p.653.
- Tremaine S. and Weinberg M.: 1984, *MNRAS*, 209, 729.
- Weinberg M.: 1985, *MNRAS*, 213, 451.
- Voglis N.: 1994 *MNRAS*, 267, 379.
- Voglis N. and Contopoulos G.: 1994, *J. Phys. A*, 27, 4899.
- Voglis N., Contopoulos G. and Efthymiopoulos C.: 1998, *Phys.Rev.E*, 57, 372.
- Voglis N., Contopoulos G. and Efthymiopoulos C.: 1999, *CeMDA*, 73, 221.
- Voglis N., Kalapotharakos C. and Stavropoulos I.: 2002, *MNRAS*, 337, 619.
- Voglis N., Stavropoulos I. and Kalapotharakos C.: 2006, *MNRAS*, 372, 901.

This paper has been typeset from a $\text{\TeX}/\text{\LaTeX}$ file prepared by the author.